ADVANCED MATERIALS
www.advmat.de

Kinetics Manipulation Enabled by Solubility Control Toward 19% Organic Solar Cells via Compatible Air Coating

Yongwen Lang, Ying Zhang, Hao Xia, Kuan Liu, Yuang Fu, Liang Han, Patrick W. K. Fong, Dongyang Li, Miao Zhang, Wai-Yeung Wong, Xinhui Lu, Tiangang Yang, Feng He,* Yang Yang, and Gang Li**

Blade coating is a promising tool for upscaling organic solar cells (OSCs). However, the performances of blade-coated OSCs still lag behind their spin-coated counterparts, limiting their competitive edge towards commercialization. One of the main reasons is that controlling the film aggregation kinetics and morphology becomes challenging during the transition from spin coating to blade coating, especially when using high boiling point solvents, which can result in excessive aggregation. Therefore, a deeper understanding and appraisal of film formation kinetics influenced by coating methods is crucial. In this work, it is demonstrated that ink solubility tuning by incorporating a twisted third component (BTP-4Cl) can induce rapid crystallization behavior and promote fine phase separation between the donor polymer (PM6) and the acceptor (BTP-eC9) in blade coating. As a result, a high power conversion efficiency (PCE) of 19.67% is obtained in OSCs (0.04 cm^2), one of the state-of-the-art efficiencies among the reported blade-coated OSCs (19.76% for the spin-coated devices). In addition, it is found that the inhibited phase aggregation contributes to enhancing the light stability of the device. This strategy offered novel insights into the effectiveness of solubility-tuning approaches for achieving highly efficient and stable OSCs under open-air coating conditions.

1. Introduction

The distinctive features of organic solar cells (OSCs), including solution processible, polychromatic, semitransparent, and roll-to-roll producible,[1–3] enable it one of the most dynamic research areas. Benefiting from the rapid evolution of organic electronic devices and materials,[4–12] the power conversion efficiencies (PCEs) of OSCs have already reached 20%.[13–16] However, the state-of-the-art PCEs were all achieved by conventional spin-coating (SC) techniques on small-area substrates,[17–20] which is not applicable to industrial production. On one hand, the solution wastage in the spin coating is inevitable.[21] On the other hand, when the substrate size is sufficiently large, the film thickness is nonuniform from the center to the edge because of the non-Newtonian effects coupled with the different radial centrifugal force distribution.[22–24] Therefore, large-area manufacturing techniques have to be developed to facilitate the commercialization of OSCs. The meniscus-guided coating (MGC) methods, including dip coating, slot-die coating, and doctor-blade coating, are good candidates for realizing high-throughput and upscaling fabrication on industrial scales. Different from the outward centrifugal and inward viscous force-controlled spin-coating methods, MGC techniques are governed by the one-directional shear force applied by the coating head and the capillary force induced by the solution's concentration and viscosity near the contact line.[25–27] The different dominant forces in

Y. Lang, Y. Zhang, H. Xia, K. Liu, P. W. K. Fong, D. Li, G. Li
The Department of Electrical and Electronic Engineering
Research Institute for Smart Energy (RISE)
Guangdong-Hong Kong-Macao Joint Laboratory for
Photonic-Thermal-Electrical Energy Materials and Devices
The Hong Kong Polytechnic University
Hong Kong 999077, China
E-mail: evazhang216@ucla.edu; gwanli@polyu.edu.hk

The ORCID identification number(s) for the author(s) of this article can be found under https://doi.org/10.1002/adma.202420096

DOI: 10.1002/adma.202420096

Y. Lang, L. Han, T. Yang, F. He
Shenzhen Grubbs Institute and Department of Chemistry
Southern University of Science and Technology
Shenzhen 518055, China
E-mail: Hef@sustech.edu.cn

Y. Zhang, Y. Yang
Department of Materials Science and Engineering
University of California
Los Angeles, LA 90095, USA

Y. Fu, X. Lu
Department of Physics
The Chinese University of Hong Kong
New Territories, Hong Kong 999077, China

M. Zhang, W.-Y. Wong
Department of Applied Biology and Chemical Technology
The Hong Kong Polytechnic University
Hung Hum Kowloon, Hong Kong 999077, China

spin-coating and MGC methods enabled different film formation mechanisms and thus different OSC film morphologies.[28,29]

To be specific, it has been validated that the solvent evaporation and the film drying time of MGC are greatly prolonged compared to that of spin-coating, with a great possibility to form oversized aggregates in the active layer.[30–32] The excessive aggregate size usually derives inferior film morphology with pronouncedly enlarged surface roughness and reduced donor/acceptor (D/A) interface area, sacrificing the charge separation, thus leading to poor fill factor (FF) and photocurrent. Therefore, The reasons for the efficiency gap from spin coating to blade coating (BC) could be summarized: 1) The long film-drying time causes the excessive phase separation domain size in blade coating[31,33–36]; 2) The relatively poor solubility of highly efficient OSC materials in non-halogenated green solvents exacerbate the agglomeration problem in blade-coating based on the Flory–Huggins model,[37–39] as large-scale production required green solvent processing due to the toxic consideration.

Several attempts were made to mitigate the excessive aggregation issues by improving the solubility when transferring from spin coating to blade coating, for example, the side chain modification strategy, which was widely used in improving the solubility of photovoltaic materials.[34,40,41] Additionally, it was reported that copolymerization strategies are also helpful in improving the solubility of OSC materials.[42,43] Although these molecular modification strategies of Y-series acceptors could help to improve the solubility, in the meantime, they also introduce uncertainties that may disrupt molecular packing and lead to undesired energy level alignment, limiting successful attempts in achieving high-efficiency devices processed from high boiling point non-halogenated solvents. Moreover, current studies in blade coating could typically ignore the correlation between solubility and material crystallization kinetics resulting from coating methods. Therefore, the evolution from solubility and film formation kinetics to final phase separation should be established to provide a clear understanding of morphology manipulation in blade-coating processes.

Here, we develop a feasible and effective multicomponent strategy to simultaneously improve the solubility and crystallization behavior enabling high-performance blade-coated devices. BTP-4Cl was selected as the third component with a twisted molecular backbone to promote the dispersion of mixed acceptors in the halogenated chlorobenzene (CB) and non-halogenated solvent o-xylene (o-XY). Upon blade coating, the more dispersed acceptors gain greater freedom to self-assemble in the solution state, promoting the formation of fast and fine crystallites in the film. This, in turn, leads to a well-controlled scale of donor-acceptor phase separation. Benefiting from the favorable phase separation nanostructure, we successfully demonstrate an excellent PCE of 19.67% via an open-air coating, which ranks among the top efficiencies in blade-coated devices. We further demonstrate that our approach applies to single green-solvent processed devices. This work not only provides valuable insights into the correlation between solubility tuning, crystallization kinetics, and device performance from the perspective of molecular structure and intermolecular interactions, providing an effective method for controlling phase separation in blade-coated OSCs, but also enables the realization of highly efficient and stable open-air-coated, eco-friendly OSCs, achieving state-of-the-art efficiencies of 19.76% for spin-coated and 19.67% for blade-coated devices.

2. Result and Discussion

2.1. Molecular Structure and Chemical Properties

To investigate the different features of SC/BC binary/ternary films, the ternary system of PM6: BTP-eC9: BTP-4Cl was employed. The chemical structures of the three materials were drawn in **Figure 1a**. Two acceptors are structure-like with the same molecular backbone but different alkyl side chains, which are expected to have good compatibility with each other to form the alloy-like phase. The energy level diagram is provided in Figure 1b. The lowest unoccupied molecular orbital (LUMO) and highest occupied molecular orbital (HOMO) of PM6, BTP-eC9, and BTP-4Cl are -3.65/-5.45, -4.05/-5.64, and -4.12/-5.68 eV, respectively.[6,5,8] The cascade energy levels guaranteed efficient charge transfer and transport in devices. Figure 1c displays the normalized ultraviolet-visible (UV-vis) absorption profile of the PM6, BTP-eC9, BTP-4Cl neat films, and BTP-eC9: BTP-4Cl blend film. PM6 showed strong absorption from 450 to 700 nm, which was complementary to the absorption of acceptors. The absorption onset of BTP-eC9, BTP-4Cl, and blend acceptor are 907.27, 943.82, and 941.43 nm, respectively, corresponding to their optical bandgaps (E_g^{opt}) of 1.37, 1.31, and 1.32 eV. The absorption coefficient of blend film was calculated by $\alpha = 2.303\ (A/t)$ to evaluate their capacity to harvest photons at certain wavelengths (Figure S1, Supporting Information), where A is absorbance and t is film thickness.[44] We found that the absorption coefficient was enhanced among the whole spectra, which was expected to contribute to higher photocurrent in ternary devices.

The contact angle (CA) measurement was performed to determine the phase separation and miscibility between active layer components (Figure S2, Supporting Information). The two-solvent method (water and ethylene glycol (EG)) was applied to determine the surface tension. The water contact angles (WCA) were measured to be 102.782°, 98.277°, 95.750°, and 95.605° for PM6, BTP-eC9, BTP-4Cl, and BTP-eC9: BTP-4Cl (0.96: 0.24), and the corresponding EG contact angles (EgCA) were measured to be 72.582°, 64.372°, 61.650°, and 62.866°. Accordingly, the surface energies were calculated to be 30.133, 36.873, 37.297, and 35.104 mN m^{-1}, respectively. The more approaching surface energy indicated the better miscibility between the donor and the mixed acceptor. The donor-acceptor interfacial energy ($\gamma_{D/A}$) and Flory-Huggins interaction parameter ($\chi_{D/A}$) were calculated and the results were listed in Table S1 (Supporting Information). The smaller the $\gamma_{D/A}$ and $\chi_{D/A}$ value, the better the miscibility between two materials.[45] The calculated $\gamma_{PM6/BTP-eC9}$, $\gamma_{PM6/BTP-4Cl}$, and $\gamma_{PM6/BTP-eC9:\ BTP-4Cl}$ are 0.680, 0.815, and 0.566 mN m^{-1}, respectively. Furthermore, $\chi_{PM6/BTP-eC9:\ BTP-4Cl}$ was calculated to be 0.190, which was smaller than $\chi_{PM6/BTP-eC9}$ and $\chi_{PM6/BTP-4Cl}$ with the value of 0.340 and 0.382, respectively, suggesting the BTP-eC9: BTP-4Cl mixed acceptor was more miscible with PM6 compared to the neat acceptor. The wetting coefficient (ω) was calculated by the equation: $\omega_{A_2} = (\gamma_{A_1/A_2} - \gamma_{D/A_2})/\gamma_{D/A_1}$ to confirm the position of the third component in the ternary blend. For $\omega_{A_2} < -1$, the third component is in the host acceptor (A_1)'s

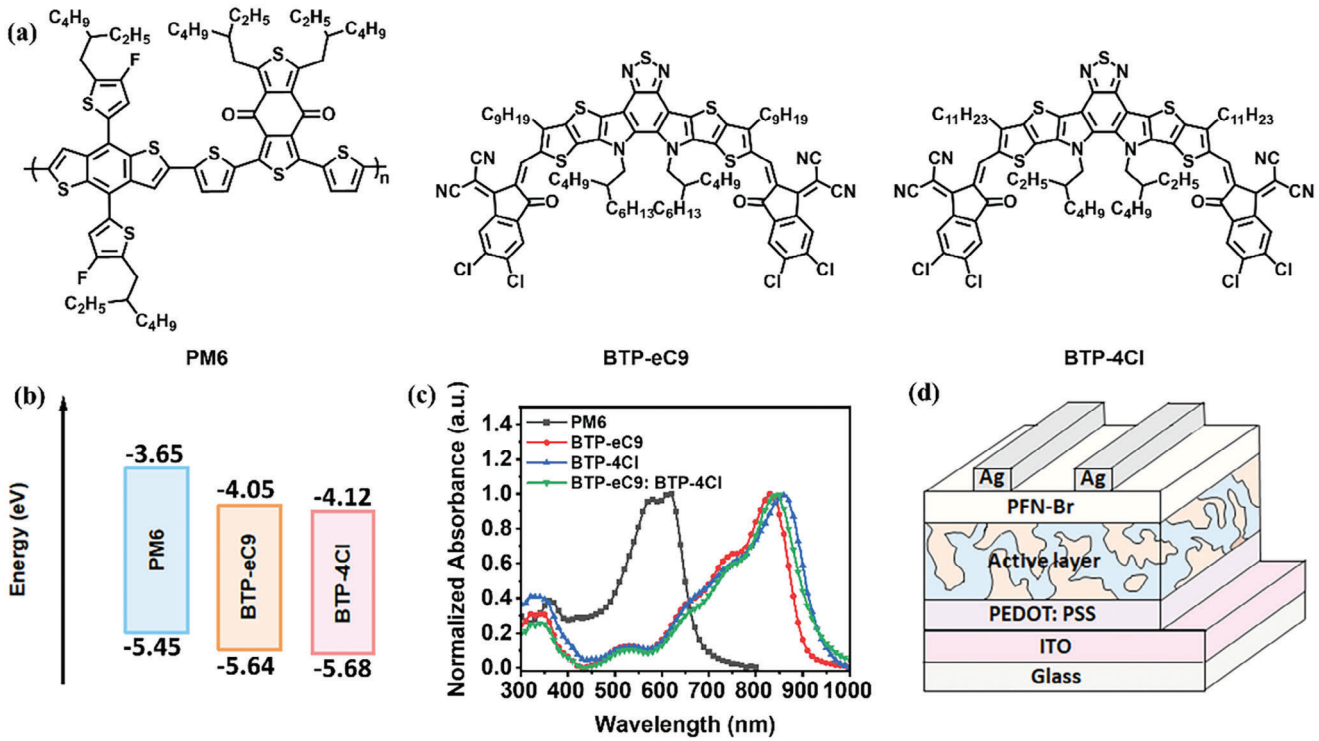

Figure 1. a) Chemical structures and b) energy levels of PM6, BTP-eC9, and BTP-4Cl. c) Normalized absorption spectra of PM6, BTP-eC9, BTP-4Cl neat film, and BTP-eC9: BTP-4Cl blend acceptor film. d) Schematic diagram of OSC device structure.

domain; for $-1 < \omega_{A_2} < 1$, the third acceptor is at the interface of donor and the host acceptor (D and A_1); for $\omega_{A_2} > -1$, the third component is in the host donor (D)'s domain.[46,47] The $\omega_{BTP-4Cl}$ was calculated to be -1.07, which indicated good compatibility between two acceptors and BTP-4Cl could easily diffuse into BTP-eC9 phases.

2.2. Device Performance and Carrier Dynamics

To investigate the device performances of SC/BC binary/ternary blends, the corresponding OSC devices were fabricated with the conventional structure of indium tin oxide (ITO)/ poly(3,4-ethylenedioxythiophene) polystyrene sulfonate (PEDOT: PSS)/active layer/ poly(9,9-bis(3′-(N,N-dimethyl)-N-ethylammoinium-propyl-2,7-fluorene)-alt-2,7-(9,9dioctylfluorene))dibromide (PFN-Br)/Ag, as shown in Figure 1d. The total donor and acceptor weight ratio was 1:1.2, and the optimized ratio of the third component in the ternary devices was 20% (Table S2, Supporting Information). The detailed device fabrication processes were provided in the supporting information. The SC-processed binary devices showed a moderate PCE of 17.92% with an open-circuit voltage (V_{OC}) of 0.848 V, a FF of 78.94%, and a short-circuit current density (J_{SC}) of 26.77 mA cm^{-2} (**Figure 2b**; **Table 1**). After the third component BTP-4Cl was added, the SC ternary devices showed a maintained V_{OC} of 0.846 V and the largely improved FF and J_{SC} with the value of 80.20% and 27.81 mA cm^{-2}, respectively, leading to an enhanced PCE of 18.87%, indicating that the participation of BTP-4Cl facilitated active layer morphology and photocurrent. The BC binary devices, however, demonstrated simultaneously declined FF (77.30%) and J_{SC} (25.90 mA cm^{-2}), leading to a lower PCE of 16.98%. It is noteworthy that the efficiency gap was effectively mitigated in BC ternary devices, which preserved a remarkable PCE of 18.62%, with a V_{OC} of 0.846 V, a FF of 79.59%, and a J_{SC} of 27.63 mA cm^{-2}, which was comparable with SC-processed ternary devices. Figure 2c depicts the external quantum efficiency (EQE) curves of corresponding devices. The integrated J_{SC} of binary devices was calculated to be 26.02 and 25.36 mA cm^{-2} for SC- and BC-processing, separately. For ternary devices, both SC- and BC-processed devices displayed high photo-responses of above 80% from 500 to 850 nm, corresponding to the integrated J_{SC} of 27.01 and 26.86 mA cm^{-2}, respectively, which were coincident with the measured J_{SC}s from *J-V* curves with all the deviations less than 3%. The result indicated that the introduction of BTP-4Cl was favorable for devices' photon utilization efficiency.

The V_{OC} and J_{SC} versus light intensity (P_{light}) were measured to estimate the charge recombination in SC and BC devices. For the trap-assisted recombination (monomolecular recombination), the relationship of $V_{OC} \propto (nkT/q)\ln P_{light}$ was applied, where n is the ideality factor, k is Boltzmann constant, q is the elementary charge, and T is Kelvin temperature. The closer the n value to 1, the more suppressed the trap-assisted recombination. Four devices gave the n value of 1.07, 1.12, 1.03, and 1.09 for SC-binary, BC-binary, SC-ternary, and BC-ternary, respectively. The relationship between J_{SC} and P_{light} followed the power law of $J_{SC} \propto P_{light}{}^{\alpha}$, where the exponential factor α could be used to evaluate the degree of bimolecular recombination – the closer the α value to 1, the more suppressed bimolecular recombination process. From

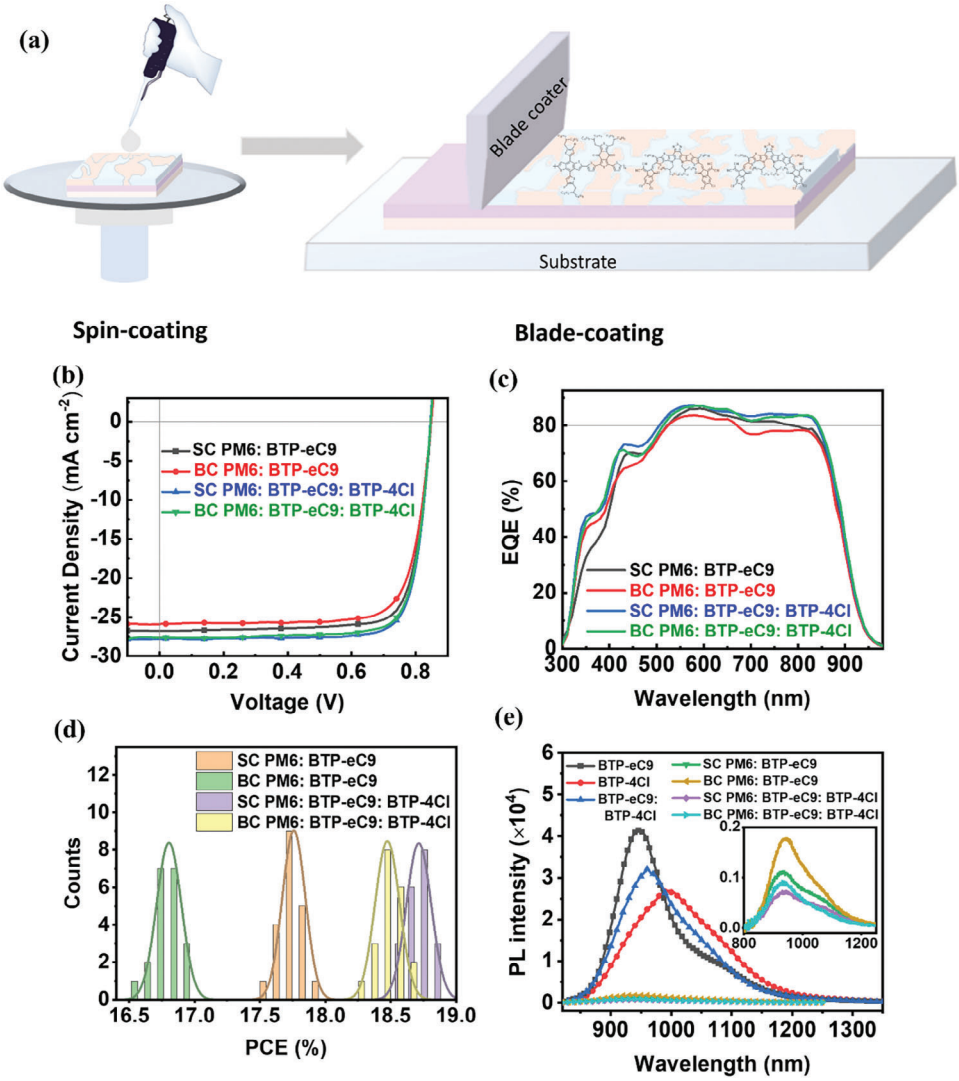

Figure 2. a) Schematic illustration of spin-coating and blade-coating deposition methods. b) *J–V* curves, c) EQE curves, and d) histograms of the optimized SC/BC binary/ternary OSCs. e) Steady-state PL spectra of neat acceptors, the mixed acceptor, and SC/BC binary/ternary blend films.

Figure S3 (Supporting Information), all devices showed weak bimolecular recombination with the α value of 0.994, 0.992, 0.994, and 0.994 for SC-binary, BC-binary, SC-ternary, and BC-ternary devices, separately. The relatively large n value and small α value for BC-binary devices implied the relatively severe charge recombination in BC-binary blends.

The charge dissociation and collection of four devices were evaluated by plotting photocurrent density (J_{ph}) versus effective voltage (V_{eff}) (Figure S4, Supporting Information), where $J_{ph} = J_{L-} J_D$ (J_L and J_D refer to the current density under illumination and in the dark), and $V_{eff} = V_{0-} V_a$ (V_0 is the voltage when J_L equals J_D and V_a is the applied voltage). When the J_{ph} is saturated (J_{sat}), it is assumed that all the excitons are dissociated into free electrons and holes. Thus, the charge dissociation (η_{diss}) and charge collection (η_{coll}) efficiency can be calculated by the ratio of J_{ph}/J_{sat} under the short-circuit condition and maximum power point, respectively. The calculated η_{diss}s are 95.88%, 93.42%, 98.43%, and 97.09% for SC PM6: BTP-eC9, BC PM6: BTP-eC9, SC PM6: BTP-eC9: BTP-4Cl, and BC PM6: BTP-eC9: BTP-4Cl devices, respectively, and the corresponding η_{coll} values were estimated to be 87.78%, 85.26%, 89.54%, and 89.33%. The much lower charge dissociation and charge collection efficiency in BC-binary devices were ascribed to the oversized pure domain sizes in the active layer, leading to limited D/A interfaces, and thus much lower FF and J_{SC}. In ternary devices, the BC-processed devices gave comparable charge dissociation and collection efficiency with SC devices, indicating the over-aggregation problem was effectively alleviated.

The steady-state photoluminescence (PL) was performed to understand the charge transfer mechanism. The excitation wavelength was determined to be 510 nm for the donor and 640 nm for acceptors. PM6 neat film exhibited a distinct maximal emission peak at ~680 nm, whose emissive profile overlapped well with two acceptors' absorption spectra, guaranteeing the ultrafast Förster resonance energy transfer process between D/A. Four blend films displayed significant PL quenching compared

Table 1. Summary of photovoltaic parameters of the spin-coated (SC) and blade-coated (BC) binary and optimized ternary OSC devices.

Active Layer	V_{OC} [V]	J_{SC} [mA cm^{-2}]	FF [%]	PCE [%]	J_{SC}^{cal} [mA cm^{-2}]
SC PM6: BTP-eC9	0.848 (0.847 ± 0.004)	26.77 (26.68 ± 0.09)	78.94 (78.84 ± 0.09)	17.92 (17.72 ± 0.09)	26.02
BC PM6: BTP-eC9	0.848 (0.847 ± 0.004)	25.90 (25.65 ± 0.13)	77.30 (77.11 ± 0.16)	16.98 (16.55 ± 0.10)	25.36
SC PM6: BTP-eC9: BTP-4Cl	0.846 (0.846 ± 0.003)	27.81 (27.67 ± 0.14)	80.20 (79.88 ± 0.18)	18.87 (18.71 ± 0.10)	27.01
BC PM6: BTP-eC9: BTP-4Cl	0.846 (0.845 ± 0.003)	27.63 (27.59 ± 0.11)	79.59 (79.44 ± 0.08)	18.62 (18.47 ± 0.09)	26.86

with neat PM6 film, while BC binary film retained residual PM6 emission peak, indicating a less efficient charge transfer process (Figure S5, Supporting Information). The PL spectra of neat acceptors and blend films are depicted in Figure 2e. BTP-eC9 neat film showed a distinctive maximal emission peak at 947 nm, and BTP-4Cl presented a relatively weaker emission at 991 nm. The mixed acceptor gave a moderate emission peak at 960 nm, indicating the energy transfer from BTP-eC9 to BTP-4Cl (Figure S5, Supporting Information). For blend films, the PL quenching efficiency was calculated to be 95.51%, 93.59%, 96.85%, and 96.64% for SC-binary, BC-binary, SC-ternary, and BC-ternary, respectively. The significantly declined PL quenching efficiency in BC binary blends was ascribed to the limited D/A interfaces resulting from excessive aggregation. It was apparent that the introduction of the third component facilitated the charge transfer efficiency, especially in blade-coated blends.

The charge transport properties were examined by the space charge limited current (SCLC) method (Figure S6; Table S6, Supporting Information). The structure of the hole-only and electron-only devices are ITO/PEDOT: PSS/active layer/Au and ITO/ZnO/active layer/Ag, respectively. The hole mobilities (μ_h) of SC PM6: BTP-eC9, BC PM6: BTP-eC9, SC PM6: BTP-eC9: BTP-4Cl, and BC PM6: BTP-eC9: BTP-4Cl-based devices are calculated to be 1.07×10^{-4}, 9.93×10^{-5}, 1.51×10^{-4}, 1.33×10^{-4} cm^{2}V^{-1}s^{-1}, and the corresponding electron mobilities (μ_e) are 1.33×10^{-4}, 1.39×10^{-4}, 1.66×10^{-4}, and 1.75×10^{-4} cm^{2}V^{-1}s^{-1}, respectively. SC devices showed much more balanced charge carrier mobility than BC devices with the μ_e/μ_h ratio of 1.24 and 1.10 for SC binary and SC ternary devices, while 1.40 and 1.32 for BC binary and BC ternary devices. The BC-processed devices were found to have relatively higher electron mobility probably due to the higher crystallinity of acceptors in BC films.

2.3. Morphological Studies

Prior to morphology analysis, we first detected the solubilities of two acceptors and the mixed acceptor in high boiling point solvent chlorobenzene to gain an initial insight into the molecular interaction between the guest and host components. The UV-vis absorption spectra of standard solutions and the diluted saturated solution are depicted in Figure S7 (Supporting Information). The maximum absorption peak was selected as the characteristic peak to fit the corresponding standard curves (Figure S8, Supporting Information). According to the fitting equation, the solubility of the neat acceptor and the mixed acceptor in CB could be calculated, which were 37.75, 37.11, and 44.47 mg mL^{-1} for BTP-eC9, BTP-4Cl, and BTP-eC9: BTP-4Cl, respectively (Table S7, Supporting Information). To elucidate the underlying mechanism behind the increased solubility, the intermolecular interactions between BTP-eC9 and BTP-4Cl molecules were analyzed based on single-crystal calculations (Figure S9, Supporting Information). Only one packing mode was detected in BTP-eC9 with the π–π distance of 3.38 Å, while distinct two packing modes were found in the mixed acceptor with a distance of 3.38 and 3.40 Å, respectively. The larger intermolecular distance indicates the more dispersed and loose molecular distribution in the mixed acceptor, which is expected to facilitate the diffusion of solvent molecules into the cavity between acceptor molecules and thus improve the solubility. Combining the larger dihedral angle of BTP-4Cl (2.70° and 4.22°) than BTP-eC9 (2.62° and 2.72°),[48] it was expected that the twisted molecular backbone would induce large steric hindrance during molecular assembly, inducing large intermolecular distance in the mixed acceptor. The dispersed molecules and improved solubility in the mixed acceptor are expected to suppress molecular aggregation to prevent oversized aggregates in blade-coated blends.[37]

Grazing incidence wide-angle X-ray scattering (GIWXAS) was performed to investigate the molecular packing and crystallinity (**Figure 3**a—d; Figure S9, Supporting Information). Through the Gauss multiple peaks fitting, the q vector and the full width at half-maximum (FWHM) of the corresponding peak were extracted to calculate the d-spacing and crystal coherent lengths (CCLs) according to the Scherrer equation, CCL = 2πK/FWHM, where K is Scherrer factor (here is 0.9). The fitting curves and the extracted parameters were summarized in Figures S11–S14 and Tables S8–S11 (Supporting Information) for the neat and blend films. PM6 demonstrated strong lamellar diffraction peaks at both in-plane (IP) and out-of-plane (OOP) directions. Different from BTP-4Cl neat film, where no apparent molecular orientation was detected, BTP-eC9 neat film exhibited preferential face-on orientation with the IP (100) peak at q_{xy} = 0.32 Å^{-1} (d-spacing = 19.63 Å and CCL = 66.53 Å) and OOP (010) peak at q_z = 1.75 Å^{-1} (d-spacing = 3.59 Å and CCL = 15.71 Å). The mixed acceptor film showed highly ordered face-on orientation with the IP lamellar peak at q_{xy} = 0.35 Å^{-1} (d-spacing = 17.95 Å and CCL = 22.53 Å) and OOP π-π peak at q_z = 1.78 Å^{-1}(d-spacing = 3.53 Å and CCL = 22.62 Å). The reduced CCL values in the IP direction but increased CCL in the OOP direction indicate a reduced alky chain stacking in BTP-eC9 along the side chain and improved long-range π–π stacking directions, which is more

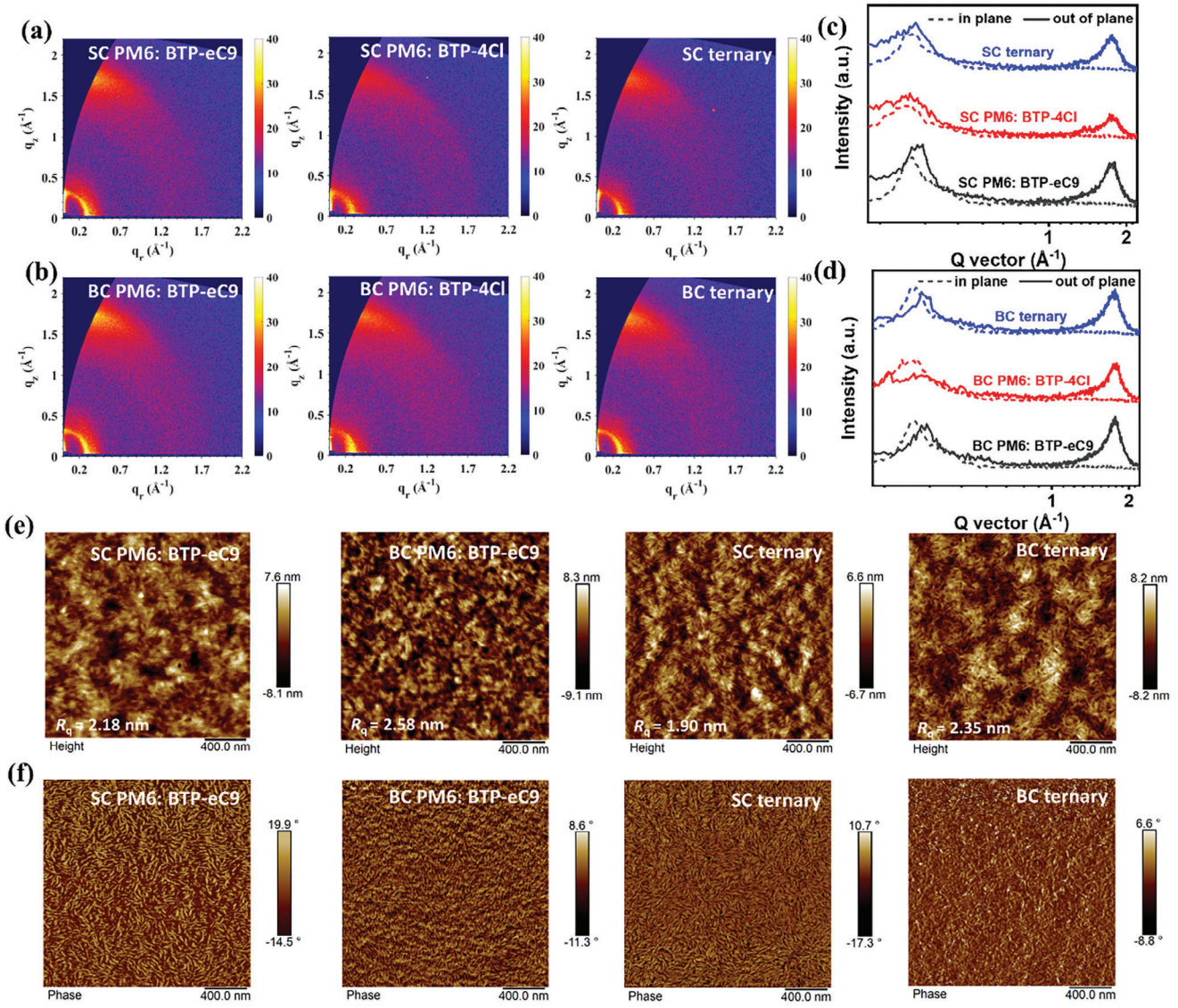

Figure 3. 2D GIWAXS patterns of a) spin-coated and b) blade-coated PM6: BTP-eC9, PM6: BTP-4Cl, and PM6: BTP-eC9: BTP-4Cl blend films. The corresponding 1D line cut profiles of c) spin-coated and d) blade-coated blend films. e) AFM height images and f) AFM phase images of SC/BC binary/ternary blend films.

favorable for charge transport. Additionally, the characteristic peak of BTP-eC9 at $q_z = 0.58$ Å^{-1} disappeared when blended with BTP-4Cl, indicating the good compatibility between two acceptors [20] and the modulation of BTP-4Cl on the organization of BTP-eC9 molecules, coincident well with the result from contact angle measurement. All blend films displayed distinct face-on orientation with representative IP (100) lamellar packing peaks and OOP (010) π-π diffraction peaks. The lamellar peaks all appeared at $\sim q_{xy} = 0.29$ Å^{-1} with a d-spacing of 21.67 Å, while the reduced CCL in ternary films indicated the reduced alkyl chain stacking via the tuning of a third component. For the OOP (010) peaks, the blade-coated binary blend gave a shorter d-spacing and a larger CCL value than the spin-coated blend, indicating the higher crystallinity (severer aggregation) in blade-coated films, which was effectively optimized by the participation of a third component, where the d-spacing retained and the increment of CCLs alleviated.

The inhibited excessive aggregation was further confirmed by Grazing-incidence small-angle X-ray scattering (GISAXS) measurement (Figures S15 and S16; Table S12, Supporting Information), where X_{DAB} represents the average correlation length of the amorphous domain and $2R_g$ represents the average length scale of pure domains, which was extracted from the Debye-Anderson-Brumberger and fractal-like network model in the fitting equation, respectively. It was noticed that the pure domain size was magnified and the mixed phases contracted from SC-film to BC-film, indicating the relatively severe aggregation in blade-coated blends. However, the pure domain size was alleviated in the BC ternary film with $2R_g$ of 25.0 nm and X_{DAB} of 31.5 nm, suggesting the effective suppression of severe aggregation by the

regulation of the third component. Additionally, the enlarged intermixing phase ensured a more efficient charge transfer efficiency in ternary blends. According to the previous result, the suppression of the excessive aggregation could be ascribed to the twisted molecular backbone of the third component.[49–51] The weakened molecular interactions between BTP-4Cl and BTP-eC9 molecules could help improve solubility and suppress phase separation in blade-coated films, enabling the formation of an optimal phase-separated length scale. This, in turn, balances charge transport and charge separation processes, leading to improved FF and J_{SC} in the optimized ternary devices.

The surface morphology was detected by tapping-mode atomic force spectroscopy (AFM) (Figure 3e,f). The root-mean-square roughness (R_q) of the SC/BC binary/ternary blends was 2.18, 2.58, 1.90, and 2.35 nm, respectively. The BC films afforded a larger R_q, while the third component effectively inhibited excessive aggregation and optimized film morphology. The nano fibrillar interpenetrating network originating from PM6 crystallization was distinctly recognized in AFM phase images, while the granular aggregates arose in BC blends, which was ascribed to the strong crystallization of Y-series acceptors. There are two dominant fibril sizes in the active layer according to their phase images (Figure S18, Supporting Information). The SC and BC binary film showed a fibril size of 19/29 nm and 20/31 nm, respectively. The ternary blend exhibited a reduced fibril size of 16/24 nm and 17/25 nm for SC and BC film, respectively. The fibril structure with a small size of ≈20 nm and an oversized domain of ≈30 nm is not favorable for efficient charge separation and charge transport. The suitable phase separation size of ≈25 nm could afford the simultaneously facilitated charge transfer and charge mobility.[16,52]

Keeping the optimized crystallinity in mind, we go ahead to investigate the effects of BTP-4Cl on BTP-eC9 in the phase transition state. It was noted that these acceptors' maximal absorption peak redshifted greatly from solution to solid film, indicating the compact molecular aggregation in films. Compared to spin-coated film, the blade-coated film exhibited a more bathochromic absorption (Figure S19, Supporting Information), suggesting that the molecular aggregation is more profound in blade-coating processing. In-situ UV–vis absorption measurement was performed to comprehend the phase transition process from solutions to solid films. The 2D contour map and the raw in-situ UV-vis absorption profiles are depicted in **Figures** 4a–d and S20 (Supporting Information). The peak position and intensity versus time were plotted by selecting their 0-0 absorption peak as the characteristic peak (Figure 4e–h). The displacement of the peak position and intensity reflected four stages during film formation, including 1) solvent evaporation, 2) preaggregation, 3) crystal growth, and 4) dried films.[3,53,54] It was noticed that the film formation mechanism was different in SC and BC films. In the solvent evaporation stage, obvious solvent evaporation was observed in spin-coating, which, however, was vague (hard to distinguish from the preaggregation stage) in blade-coating due to lower shear force and Reynold number.[25–27] In the preaggregation stage, the time duration was much longer and the preaggregation rate was much slower in blade-coating, explaining the severe aggregation in BC blends. In the crystal growth stage, apparent peak redshift along with an abrupt change of peak intensity was observed in both the spin- and blade-coating process due to the ordered and compact molecular aggregation from solution to solid film.

The role of the third component in regulating molecular aggregation behavior during phase transition was investigated. It was found that the solvent evaporation time was abbreviated and the solvent evaporation rate was accelerated in ternary blends (Figure S21, Supporting Information), indicating that the third component could facilitate the solvent removal and promote film solidifying. In the preaggregation stage, given the relatively poor solubility of BTP-4Cl and the solvent removal function, the BTP-4Cl was considered to first reach the solubility limit and crystallize.[19] The crystalized BTP-4Cl provides the nuclei seeding sites enabling the advanced onset of crystalline than in the binary system. Additionally, the more dispersed molecular distribution in the solution enabled more dispersed seeding sites during phase transition, leading to a much-shortened preaggregation time and finer crystal grains. In the crystal growth stage, ternary blends underwent earlier and faster crystal growth, which was ascribed to the larger amount and more dispersed pre-aggregates, enabling a faster crystal growth rate and finer phase domain. Furthermore, the dispersed and loose molecular distribution along with the enhanced solubility ensured sufficient time for order and favorable molecular reassembly during film formation. Thus, finer and higher-quality crystallites were expected in the blade-coated ternary blends.

Based on ex situ and in situ morphological results, we propose a visualized crystallization landscape that illustrates how BTP-4Cl enables the self-assembly of BTP-eC9 when processed from high-boiling-point solvents during blade coating (**Figure** 5g). In the solution state (preaggregation stage), the twisted molecular backbone of BTP-4Cl promotes a more dispersed and loose molecular distribution within the ternary solution, improving solubility and preventing excessive preaggregation. During the crystallization process, BTP-4Cl aids in promoting solvent removal, shortening crystallization time, accelerating crystallization, and facilitating the formation of fine and high-quality crystallites in the blade-coated blends. As a result, we achieved an ordered microstructure with well-defined donor and acceptor domains, leading to optimized crystallinity with a preferred face-on orientation.

2.4. Stability and Generality Test

Light stability was measured to evaluate the capability of four blends to resist light-induced degradation (Figure 5a). All blends showed a burn-in loss in the first 100 h and were then kept stable with the T_{80} > 500 h under continuous illumination in a glovebox under nitrogen. After the third component was added, the photostability was improved in both SC and BC devices, which could be ascribed to the locking-in morphology effect of the third component.[55] It was found that the light stability of SC devices was superior to that of BC devices, where SC devices tended to have a faster J_{SC} decay and BC devices tended to have a quicker V_{OC} and FF degradation (Figure S22, Supporting Information). One possible explanation is that during the formation of BC film, the slow film formation and air atmosphere would induce more traps in blends, which is a potential crisis for BC films' stability. For SC films, however, the D/A intermixing phases are larger

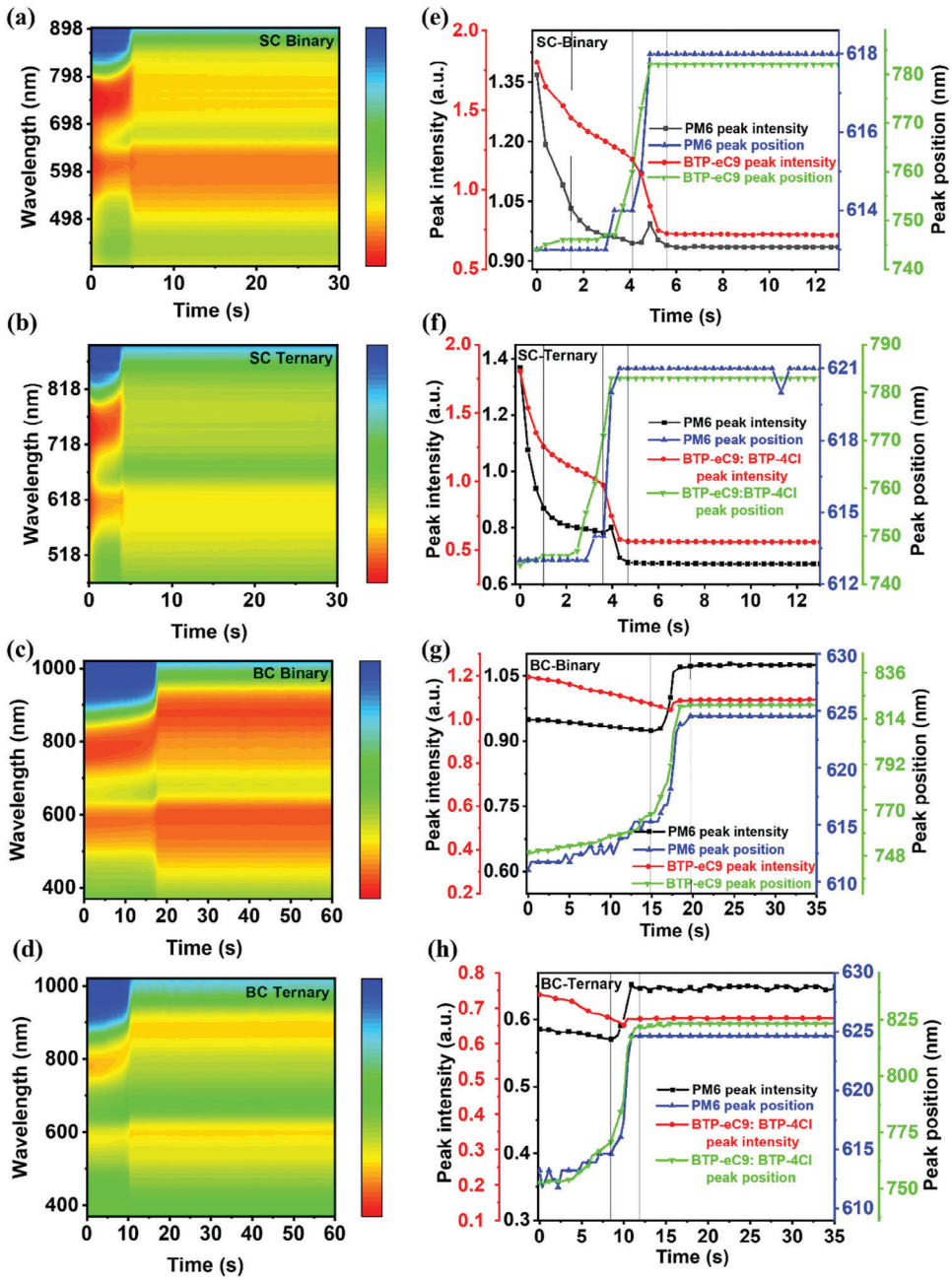

Figure 4. In situ UV–vis absorption measurement. The contour map of a) SC binary film, b) SC ternary film, c) BC binary film, and d) BC ternary film. The donor and acceptor peak position and peak intensity versus time for e) SC binary film, f) SC ternary film, g) BC binary film, and h) BC ternary film.

than that in BC films, with a greater possibility of de-mixing between donor and acceptor, leading to deteriorated J_{SC}s. Thus, we would infer that SC devices have a severer morphological degradation and BC devices have a severer defect-induced loss.[56,57] However, further research was needed to figure out their photodegradation mechanism.

The suppression of excessive aggregation in blade coating via the ternary strategy was further confirmed by the green solvent-processed OSCs and upscaling devices (1cm^2). When changing the processing solvent from chlorobenzene (0.5% DIO) to single component green solvent o-XY (Figure S23, Supporting Information), the SC binary devices displayed a moderate PCE of 16.01%, while that of BC binary devices was 15.55% resulting from the decreased FF and J_{SC}. However, such a downward trend was effectively suppressed by introducing BTP-4Cl. SC ternary and BC ternary devices showed comparable PCE of 16.85% and 16.71% (Table S13, Supporting Information). When magnifying the device area to 1 cm^2 (Figure 5b), SC binary devices gave a PCE of 15.75% (FF = 71.81%, and J_{SC} = 25.98 mA cm^{-2}.) and BC binary devices showed a lagged PCE of 15.12%, resulting from the inferior FF (70.64%) and J_{SC} (25.34 mA cm^{-2}). However, in ternary devices, the SC and BC devices manifested comparable

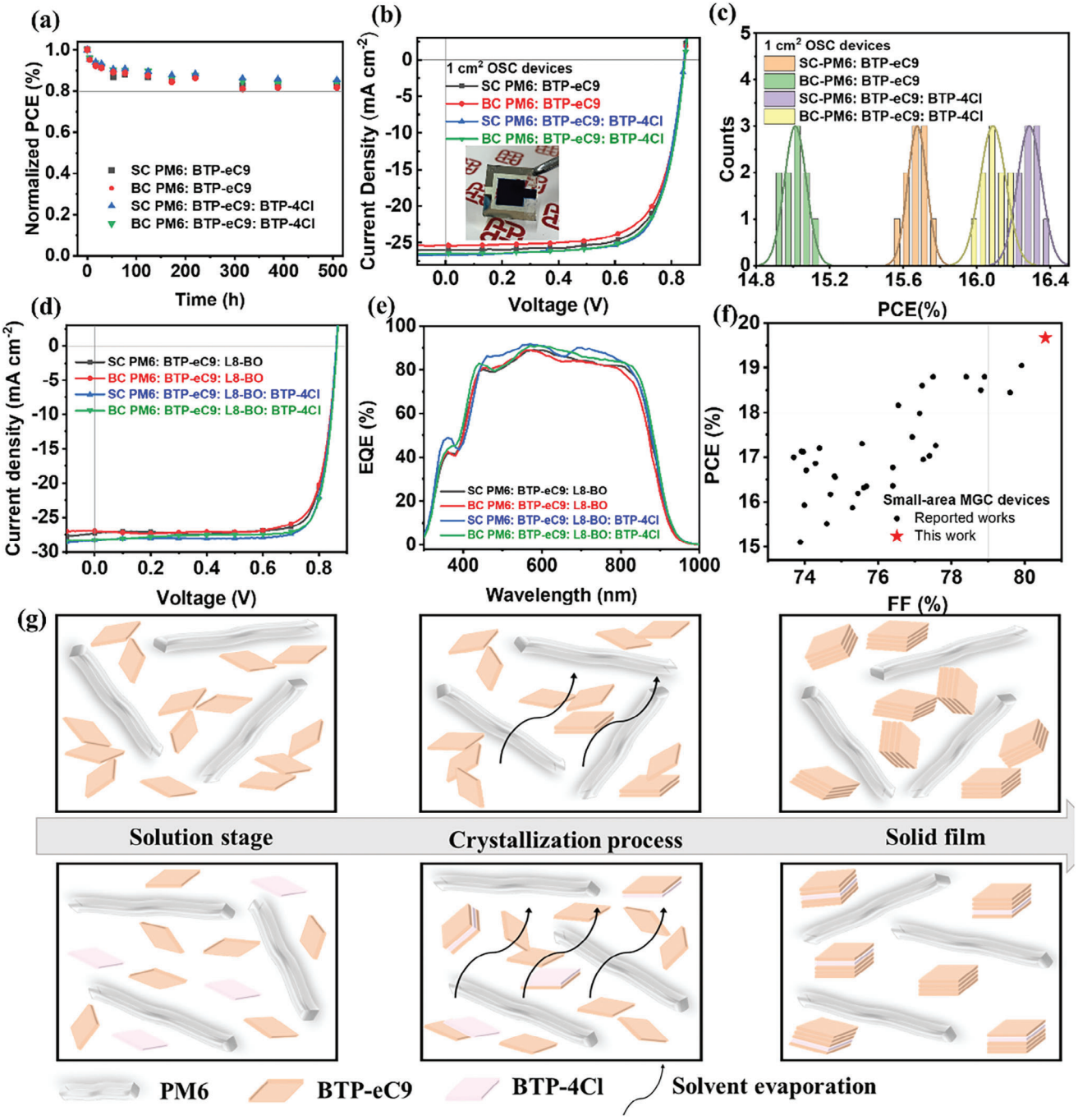

Figure 5. a) Light stability of SC/BC binary/ternary OSCs. b) *J–V* curves and c) histograms of the optimized 1 cm^2 SC/BC binary/ternary OSCs. d) *J–V* curves and e) EQE curves of the optimized ternary/quaternary OSCs. f) Summary of the representative MGC OSCs with area smaller than 0.1 cm^2. g) Schematic crystallization process in the binary and ternary film.

photovoltaic parameters with a PCE of 16.40% and 16.19%, respectively (Table S14, Supporting Information).

This morphology-tuning strategy was demonstrated on other photoactive layer components, the ternary component of PM6: eC9-2Cl: BTP-4Cl and the quaternary component of PM6: BTP-eC9: L8-BO: BTP-4Cl. The optimized ratio of BTP-4Cl was shown in Tables S15 and S17 (Supporting Information), respectively. The device efficiency increased with the optimized ratio of BTP-4Cl thanks to the enhanced FFs and J_{SC}s. Compared with PM6: eC9-2Cl binary devices, BTP-4Cl-based ternary devices showed good tolerance by different processing methods (Table S16, Supporting Information), consistent with previous results. This trend maintained in the quaternary devices that BTP-4Cl alleviated the efficiency gap from spin-coating to blade-coating. The

Table 2. Summary of photovoltaic parameters of the spin-coated (SC) and blade-coated (BC) ternary and optimized quaternary OSC devices.

Active Layer	V_{OC} [V]	FF [%]	J_{SC} [mA cm^{-2}]	PCE [%]	J_{SC}^{cal} [mA cm^{-2}]
SC PM6: BTP-eC9: L8-BO	0.862 (0.861 ± 0.004)	80.46 (80.10 ± 0.45)	27.34 (27.45 ± 0.18)	18.96 (18.93 ± 0.05)	26.61
BC PM6: BTP-eC9: L8-BO	0.862 (0.865 ± 0.003)	79.59 (79.42 ± 0.47)	26.98 (26.90 ± 0.20)	18.51 (18.48 ± 0.06)	26.17
SC PM6: BTP-eC9: L8-BO: BTP-4Cl	0.862 (0.860 ± 0.003)	80.89 (80.67 ± 0.49)	28.34 (28.31 ± 0.20)	19.76 (19.68 ± 0.05)	27.64
BC PM6: BTP-eC9: L8-BO: BTP-4Cl	0.863 (0.861 ± 0.002)	80.56 (80.48 ± 0.50)	28.29 (28.26 ± 0.23)	19.67 (19.56 ± 0.06)	27.51

SC-PM6: BTP-eC9: L8-BO gave a PCE of 18.96%, while the BC processed devices dropped to 18.51% due to the lower FF and J_{SC}. However, the quaternary devices maintained well in both SC and BC devices. The SC quaternary devices exhibited an optimal FF of 80.89% and PCE of 19.76%. Comparably, the BC-processed devices gave a PCE of 19.67% with an outstanding FF of 80.56% (Figure 5d; **Table 2**), which was the highest efficiency among blade-coating processed small-area (<0.1cm^2) devices [3,17,21,27,29,39,58–72] (Figure 5f; Table S18, Supporting Information). The greatly improved device performance is ascribed to the incorporation of L8-BO facilitating the formation of hierarchical morphology with both parallel and alloy-like structures, which is believed to enhance charge transport and charge separation, ultimately contributing to improved device performance.[46,73]

3. Conclusion

To summarize, we developed a solubility-tuning strategy via multi-component to manipulate crystallization kinetics and aggregate sizes to achieve well-behaved phase separation in blade-coated blends. By incorporating BTP-4Cl, both ex-situ and in-situ investigations illustrated that the twisted molecular backbone of BTP-4Cl facilitates a dispersed and loose molecular distribution in the ternary solution. This leads to the formation of dispersed nuclei seeding sites and pre-aggregates, thereby advancing the crystallization process and achieving fine nanoscale phase domains. As a result, the blade-coated small-area OSCs achieved an outstanding PCE of 19.67% (19.76% for SC devices), which is the top-ranking efficiency among reported blade-coated OSCs. Overall, this work gave a new insight into the material selection criteria from the point of solubility control, and established the correlation between solubility, crystallization kinetics, and solid film microstructure, providing valuable guidance for achieving stable and high-performance eco-OSCs via open-air coating.

Supporting Information

Supporting Information is available from the Wiley Online Library or from the author.

Acknowledgements

This work was supported by the Research Grants Council of Hong Kong (Project Nos. C7018-20G, C4005-22Y, the RGC Senior Research Fellowship Scheme (SRFS2223-5S01)), the Hong Kong Polytechnic University (Sir Sze-yuen Chung Endowed Professorship Fund (8-8480), RISE (Q-CDBK), PRI (Q-CD7X)), Guangdong-Hong Kong-Macao Joint Laboratory for Photonic-Thermal-Electrical Energy Materials and Devices (GDSTC No. 2019B121205001, the National Natural Science Foundation of China (22225504).

Conflict of Interest

The authors declare no conflict of interest.

Data Availability Statement

The data that support the findings of this study are available from the corresponding author upon reasonable request.

Keywords

blade coating, crystallization kinetics, organic solar cells, solubility-tuning

Received: December 20, 2024
Revised: February 6, 2025
Published online: February 23, 2025

[1] G. Li, R. Zhu, Y. Yang, *Nat. Photonics* **2012**, *6*, 153.
[2] G. Li, V. Shrotriya, J. Huang, Y. Yao, T. Moriarty, K. Emery, Y. Yang, *Nat. Mater.* **2005**, *4*, 864.
[3] Y. Zhang, K. Liu, J. Huang, X. Xia, J. Cao, G. Zhao, P. W. K. Fong, Y. Zhu, F. Yan, Y. Yang, X. Lu, G. Li, *Nat. Commun.* **2021**, *12*, 4815.
[4] J. Yuan, Y. Zhang, L. Zhou, G. Zhang, H.-L. Yip, T.-K. Lau, X. Lu, C. Zhu, H. Peng, P. A. Johnson, M. Leclerc, Y. Cao, J. Ulanski, Y. Li, Y. Zou, *Joule* **2019**, *3*, 1140.
[5] Y. Cui, H. Yao, J. Zhang, K. Xian, T. Zhang, L. Hong, Y. Wang, Y. Xu, K. Ma, C. An, C. He, Z. Wei, F. Gao, J. Hou, *Adv. Mater.* **2020**, *32*, 1908205.
[6] Y. Cui, H. Yao, J. Zhang, T. Zhang, Y. Wang, L. Hong, K. Xian, B. Xu, S. Zhang, J. Peng, Z. Wei, F. Gao, J. Hou, *Nat. Commun.* **2019**, *10*, 2515.
[7] H. Lai, Q. Zhao, Z. Chen, H. Chen, P. Chao, Y. Zhu, Y. Lang, N. Zhen, D. Mo, Y. Zhang, F. He, *Joule* **2020**, *4*, 688.
[8] M. Zhang, X. Guo, W. Ma, H. Ade, J. Hou, *Adv. Mater.* **2015**, *27*, 4655.
[9] Q. Liua, Y. Jiang, K. Jin, J. Qin, J. Xu, W. Li, J. Xiong, J. Liu, Z. Xiao, K. Sun, S. Yang, X. Zhang, L. Ding, *Sci. Bull* **2020**, *65*, 272.
[10] H. Yin, C. Yan, H. Hu, J. K. W. Ho, X. Zhan, G. Li, S. K. So, *Mater. Sci. Eng. R Rep.* **2020**, *140*, 100542.
[11] Q. Fan, R. Ma, Z. Bi, X. Liao, B. Wu, S. Zhang, W. Su, J. Fang, C. Zhao, C. Yan, K. Chen, Y. Li, C. Gao, G. Li, W. Ma, *Adv. Funct. Mater.* **2023**, *33*, 2211385.

[12] Z. Xu, S.-H. Li, L. Ma, G. Li, Y. Yang, *Appl. Phys. Lett.* **2007**, *91*, 092911.
[13] Z. Zheng, J. Wang, P. Bi, J. Ren, Y. Wang, Y. Yang, X. Liu, S. Zhang, J. Hou, *Joule* **2022**, *6*, 171.
[14] Y. Cui, Y. Xu, H. Yao, P. Bi, L. Hong, J. Zhang, Y. Zu, T. Zhang, J. Qin, J. Ren, Z. Chen, C. He, X. Hao, Z. Wei, J. Hou, *Adv. Mater.* **2021**, *33*, 2102420.
[15] J. Fu, P. W. K. Fong, H. Liu, C.-S. Huang, X. Lu, S. Lu, M. Abdelsamie, T. Kodalle, C. M. Sutter-Fella, Y. Yang, G. Li, *Nat. Commun.* **2023**, *14*, 1760.
[16] P. Bi, J. Wang, Y. Cui, J. Zhang, T. Zhang, Z. Chen, J. Qiao, J. Dai, S. Zhang, X. Hao, Z. Wei, J. Hou, *Adv. Mater.* **2023**, *35*, 2210865.
[17] Y. Zhang, W. Deng, C. E. Petoukhoff, X. Xia, Y. Lang, H. Xia, H. Tang, H. T. Chandran, S. Mahadevan, K. Liu, P. W. K. Fong, Y. Luo, J. Wu, S.-W. Tsang, F. Laquai, H. Wu, X. Lu, Y. Yang, G. Li, *Joule* **2024**, *8*, 509.
[18] L. Zhu, M. Zhang, G. Zhou, Z. Wang, W. Zhong, J. Zhuang, Z. Zhou, X. Gao, L. Kan, B. Hao, F. Han, R. Zeng, X. Xue, S. Xu, H. Jing, B. Xiao, H. Zhu, Y. Zhang, F. Liu, *Joule* **2024**, *8*, 3153.
[19] R. Zeng, M. Zhang, X. Wang, L. Zhu, B. Hao, W. Zhong, G. Zhou, J. Deng, S. Tan, J. Zhuang, F. Han, A. Zhang, Z. Zhou, X. Xue, S. Xu, J. Xu, Y. Liu, H. Lu, X. Wu, C. Wang, Z. Fink, T. P. Russell, H. Jing, Y. Zhang, Z. Bo, F. Liu, *Nat Energy* **2024**, *9*, 1117.
[20] Y. Lang, H. Lai, Y. Fu, R. Ma, P. W. K. Fong, H. Li, K. Liu, X. Yang, X. Lu, T. Yang, G. Li, F. He, *Adv. Mater.* **2025**, *37*, 2413270.
[21] J. Wan, Y. Wu, R. Sun, J. Qiao, X. Hao, J. Min, *Energy Environ. Sci.* **2022**, *15*, 5192.
[22] S. Liu, D. Chen, X. Hu, Z. Xing, J. Wan, L. Zhang, L. Tan, W. Zhou, Y. Chen, *Adv. Funct. Mater.* **2020**, *30*, 2003223.
[23] J. A. Britten, I. M. Thomas, *J. Appl. Phys.* **1992**, *71*, 972.
[24] P. C. Sukanek, *J. Electrochem. Soc.* **1991**, *138*, 1712.
[25] X. Gu, L. Shaw, K. Gu, M. F. Toney, Z. Bao, *Nat. Commun.* **2018**, *9*, 534.
[26] H. Li, S. Liu, X. Wu, Q. Qi, H. Zhang, X. Meng, X. Hu, L. Ye, Y. Chen, *Energy Environ. Sci.* **2022**, *15*, 2130.
[27] J. Yuan, D. Liu, H. Zhao, B. Lin, X. Zhou, H. B. Naveed, C. Zhao, K. Zhou, Z. Tang, F. Chen, W. Ma, *Adv. Energy Mater.* **2021**, *11*, 2100098.
[28] H. W. Ro, J. M. Downing, S. Engmann, A. A. Herzing, D. M. DeLongchamp, L. J. Richter, S. Mukherjee, H. Ade, M. Abdelsamie, L. K. Jagadamma, A. Amassian, Y. Liu, H. Yan, *Energy Environ. Sci.* **2016**, *9*, 2835.
[29] J. Xue, H. B. Naveed, H. Zhao, B. Lin, Y. Wang, Q. Zhu, B. Wu, Z. Bi, X. Zhou, C. Zhao, K. Zhou, W. Ma, *J. Mater. Chem. A* **2022**, *10*, 13439.
[30] L. Zhang, B. Lin, B. Hu, X. Xu, W. Ma, *Adv. Mater.* **2018**, *30*, 1800343.
[31] W. Zhao, S. Zhang, Y. Zhang, S. Li, X. Liu, C. He, Z. Zheng, J. Hou, *Adv. Mater.* **2018**, *30*, 1704837.
[32] Z. Peng, Y. Zhang, X. Sun, W. Zhao, F. Bian, Y. Geng, L. Ye, C. Yang, *Adv. Funct. Mater.* **2023**, *33*, 2213248.
[33] D. Chen, S. Liu, B. Huang, J. Oh, F. Wu, J. Liu, C. Yang, L. Chen, Y. Chen, *Small* **2022**, *18*, 2200734.
[34] S. Dong, T. Jia, K. Zhang, J. Jing, F. Huang, *Joule* **2020**, *4*, 2004.
[35] W. Zhao, Y. Zhang, S. Zhang, S. Li, C. He, J. Hou, *J. Mater. Chem. C* **2019**, *7*, 3206.
[36] F. Liu, S. Ferdous, E. Schaible, A. Hexemer, M. Church, X. Ding, C. Wang, T. P. Russell, *Adv. Mater.* **2015**, *27*, 886.
[37] H. Chen, R. Zhang, X. Chen, G. Zeng, L. Kobera, S. Abbrent, B. Zhang, W. Chen, G. Xu, J. Oh, S.-H. Kang, S. Chen, C. Yang, J. Brus, J. Hou, F. Gao, Y. Li, Y. Li, *Nat. Energy* **2021**, *6*, 1045.
[38] H. Chen, W. Sun, R. Zhang, Y. Huang, B. Zhang, G. Zeng, J. Ding, W. Chen, F. Gao, Y. Li, Y. Li, *Adv. Mater.* **2024**, *36*, 2402350.
[39] H. Bai, R. Ma, W. Su, T. A. D. Peña, T. Li, L. Tang, J. Yang, B. Hu, Y. Wang, Z. Bi, Y. Su, Q. Wei, Q. Wu, Y. Duan, Y. Li, J. Wu, Z. Ding, X. Liao, Y. Huang, C. Gao, G. Lu, M. Li, W. Zhu, G. Li, Q. Fan, W. Ma, *Nano-Micro Lett.* **2023**, *15*, 241.
[40] L. Hong, H. Yao, Z. Wu, Y. Cui, T. Zhang, Y. Xu, R. Yu, Q. Liao, B. Gao, K. Xian, H. Y. Woo, Z. Ge, J. Hou, *Adv. Mater.* **2019**, *31*, 1903441.
[41] Y. Cui, H. Yao, L. Hong, T. Zhang, Y. Tang, B. Lin, K. Xian, B. Gao, C. An, P. Bi, W. Ma, J. Hou, *Natl. Sci. Rev.* **2020**, *7*, 1239.
[42] Y. Cui, H. Yao, L. Hong, T. Zhang, Y. Xu, K. Xian, B. Gao, J. Qin, J. Zhang, Z. Wei, J. Hou, *Adv. Mater.* **2019**, *31*, 1808356.
[43] S. Rasool, D. V. Vu, C. E. Song, H. K. Lee, S. K. Lee, J.-C. Lee, S.-J. Moon, W. S. Shin, *Adv. Energy Mater.* **2019**, *9*, 1900168.
[44] R. Rai, B. K. Singh, Absorbance and Transmittance Measurement of CsI Thin FIlms, Bhabha Atomic Research Centre, **2013**, 838.
[45] H. Xia, Y. Zhang, W. Deng, K. Liu, X. Xia, C.-J. Su, U.-S. Jeng, M. Zhang, J. Huang, J. Huang, C. Yan, W.-Y. Wong, X. Lu, W. Zhu, G. Li, *Adv. Mater.* **2022**, *34*, 2107659.
[46] L. Zhan, S. Yin, Y. Li, S. Li, T. Chen, R. Sun, J. Min, G. Zhou, H. Zhu, Y. Chen, J. Fang, C.-Q. Ma, X. Xia, X. Lu, H. Qiu, W. Fu, H. Chen, *Adv. Mater.* **2022**, *34*, 2206269.
[47] T. Liu, T. Yang, R. Ma, L. Zhan, Z. Luo, G. Zhang, Y. Li, K. Gao, Y. Xiao, J. Yu, X. Zou, H. Sun, M. Zhang, T. A. Dela Peña, Z. Xing, H. Liu, X. Li, G. Li, J. Huang, C. Duan, K. S. Wong, X. Lu, X. Guo, F. Gao, H. Chen, F. Huang, Y. Li, Y. Li, Y. Cao, B. Tang, et al., *Joule* **2021**, *5*, 914.
[48] H. Lai, H. Chen, Z.-Y. Chen, Y. Lang, Y. Zhu, S.-T. Zhang, X. Lai, P. Tan, Y. Zhang, B. Yang, G. Li, F. He, *Energy Environ. Sci.* **2023**, *16*, 5944.
[49] W. Zhou, J. Liu, J. Xie, S. You, J. Deng, F. Yu, S. Y. Jeong, H. Y. Woo, F. Wu, L. Chen, *Angew. Chem., Int. Ed.* **2025**, *64*, 202415141.
[50] J. Song, C. Zhang, C. Li, J. Qiao, J. Yu, J. Gao, X. Wang, X. Hao, Z. Tang, G. Lu, R. Yang, H. Yan, Y. Sun, *Angew. Chem., Int. Ed.* **2024**, *63*, 202404297.
[51] X. Liao, Q. Xie, Y. Guo, Q. He, Z. Chen, N. Yu, P. Zhu, Y. Cui, Z. Ma, X. Xu, H. Zhu, Y. Chen, *Energy Environ. Sci.* **2022**, *15*, 384.
[52] L. Zhu, M. Zhang, J. Xu, C. Li, J. Yan, G. Zhou, W. Zhong, T. Hao, J. Song, X. Xue, Z. Zhou, R. Zeng, H. Zhu, C.-C. Chen, R. C. I. MacKenzie, Y. Zou, J. Nelson, Y. Zhang, Y. Sun, F. Liu, *Nat. Mater.* **2022**, *21*, 656.
[53] R. Ma, C. Yan, P. W.-K. Fong, J. Yu, H. Liu, J. Yin, J. Huang, X. Lu, H. Yan, G. Li, *Energy Environ. Sci.* **2022**, *15*, 2479.
[54] B. Lin, X. Zhou, H. Zhao, J. Yuan, K. Zhou, K. Chen, H. Wu, R. Guo, M. A. Scheel, A. Chumakov, S. V. Roth, Y. Mao, L. Wang, Z. Tang, P. Müller-Buschbaum, W. Ma, *Energy Environ. Sci.* **2020**, *13*, 2467.
[55] S. Jung, Y. Cho, S.-H. Kang, S.-J. Yoon, C. Yang, *Sol. RRL* **2022**, *6*, 2100819.
[56] E. M. Speller, A. J. Clarke, J. Luke, H. K. H. Lee, J. R. Durrant, N. Li, T. Wang, H. C. Wong, J.-S. Kim, W. C. Tsoi, Z. Li, *J. Mater. Chem. A* **2019**, *7*, 23361.
[57] A. Kumar, R. Devine, C. Mayberry, B. Lei, G. Li, Y. Yang, *Adv. Funct. Mater.* **2010**, *20*, 2729.
[58] R. Sun, Q. Wu, J. Guo, T. Wang, Y. Wu, B. Qiu, Z. Luo, W. Yang, Z. Hu, J. Guo, M. Shi, C. Yang, F. Huang, Y. Li, J. Min, *Joule* **2020**, *4*, 407.
[59] P. Wang, J. Zhang, D. Luo, J. Xue, L. Zhang, H. Mao, Y. Wang, C. Yu, W. Ma, Y. Chen, *Adv. Funct. Mater.* **2024**, *34*, 2402680.
[60] Y. Li, H. Liu, J. Wu, H. Tang, H. Wang, Q. Yang, Y. Fu, Z. Xie, *ACS Appl. Mater. Interfaces* **2021**, *13*, 10239.
[61] L. Liu, B. Yu, L. Kang, W. Deng, X. Zhao, *Adv. Funct. Mater.* **2023**, *33*, 2214781.
[62] G. Park, Y. Cho, S. Jeong, J. Park, S.-J. Yoon, C. Yang, *J. Mater. Chem. A* **2023**, *11*, 12185.
[63] L. Zhang, Y. He, W. Deng, X. Guo, Z. Bi, J. Zeng, H. Huang, G. Zhang, C. Xie, Y. Zhang, X. Hu, W. Ma, Y. Yuan, X. Yuan, *Discov. Nano* **2024**, *19*, 39.
[64] J.-Y. Fan, Z.-X. Liu, J. Rao, K. Yan, Z. Chen, Y. Ran, B. Yan, J. Yao, G. Lu, H. Zhu, C.-Z. Li, H. Chen, *Adv. Mater.* **2022**, *34*, 2110569.
[65] Q. Wu, W. Wang, Y. Wu, Z. Chen, J. Guo, R. Sun, J. Guo, Y. (Michael) Yang, J. Min, *Adv. Funct. Mater.* **2021**, *31*, 2010411.
[66] R. Sun, T. Wang, X. Yang, Y. Wu, Y. Wang, Q. Wu, M. Zhang, C. J. Brabec, Y. Li, J. Min, *Nat. Energy* **2022**, *7*, 1087.
[67] Y. Yu, R. Sun, T. Wang, X. Yuan, Y. Wu, Q. Wu, M. Shi, W. Yang, X. Jiao, J. Min, *Adv. Funct. Mater.* **2021**, *31*, 2008767.

[68] H. Zhao, B. Lin, J. Xue, H. B. Naveed, C. Zhao, X. Zhou, K. Zhou, H. Wu, Y. Cai, D. Yun, Z. Tang, W. Ma, *Adv. Mater.* **2022**, *34*, 2105114.
[69] J. Xue, H. Zhao, B. Lin, Y. Wang, Q. Zhu, G. Lu, B. Wu, Z. Bi, X. Zhou, C. Zhao, G. Lu, K. Zhou, W. Ma, *Adv. Mater.* **2022**, *34*, 2202659.
[70] K. Weng, L. Ye, L. Zhu, J. Xu, J. Zhou, X. Feng, G. Lu, S. Tan, F. Liu, Y. Sun, *Nat. Commun.* **2020**, *11*, 2855.
[71] J. Zhang, H. Mao, K. Zhou, L. Zhang, D. Luo, P. Wang, L. Ye, Y. Chen, *Adv. Mater.* **2024**, *36*, 2309379.
[72] J. Zhang, L. Zhang, X. Wang, Z. Xie, L. Hu, H. Mao, G. Xu, L. Tan, Y. Chen, *Adv. Energy Mater.* **2022**, *12*, 2200165.
[73] L. Arunagiri, Z. Peng, X. Zou, H. Yu, G. Zhang, Z. Wang, J. Y. Lin Lai, J. Zhang, Y. Zheng, C. Cui, F. Huang, Y. Zou, K. S. Wong, P. C. Y. Chow, H. Ade, H. Yan, *Joule* **2020**, *4*, 1790.